JACS Au
AN OPEN ACCESS JOURNAL OF THE AMERICAN CHEMICAL SOCIETY

pubs.acs.org/jacsau
Article

Unveiling the Nanocluster Conversion Pathway for Highly Monodisperse InAs Colloidal Quantum Dots

Jibin Shin,[#] Mahnmin Choi,[#] Doeun Shim, Tyler Joe Ziehl, Seongmin Park, Eunhye Cho, Peng Zhang, Hangil Lee, Joongoo Kang, and Sohee Jeong*

Cite This: JACS Au 2024, 4, 1097−1106
Read Online

ACCESS | Metrics & More | Article Recommendations | Supporting Information

ABSTRACT: Colloidal quantum dots (CQDs) have garnered significant attention in nanoscience and technology, with a particular emphasis on achieving high monodispersity in their synthesis. Recent advances in understanding the chemistry of reaction intermediates such as magic-sized nanoclusters (MSC) have paved the way for innovative synthetic strategies. Notably, monodisperse CQDs of various compositions, including indium phosphide, indium arsenide, and cadmium chalcogenide, have been successfully prepared using nanocluster intermediates as single-source precursors. Still, the early stage conversion chemistry of these nanoclusters preceding CQD formation has not been fully unveiled yet. Herein, we report the first-order conversion of amorphous nanoclusters (AMCs) to InAs MSCs prior to the formation of CQDs. We find that MSC, isolated via gel-permeation chromatography, is more stable than purified AMCs, as demonstrated in various chemical and thermolytic reactions. While the surface of InAs AMCs and MSC is similarly bound with carboxylate ligands, detailed structural analyses employing synchrotron X-ray scattering and X-ray absorption spectroscopy unveil subtle distinctions arising from the distinct surface properties and structural disorder characteristics of InAs nanoclusters. We propose that InAs AMCs undergo a surface reduction and structural ordering process, resulting in the formation of an InAs MSC in a thermodynamically local minimum state. Furthermore, we demonstrate that both types of nanoclusters serve as viable precursors, providing a similar monomer supply rate at elevated temperatures of around 300 °C. This study offers invaluable insights into the interplay of structure and chemical stability in binary nanoclusters, enhancing our ability to design these nanoclusters as precursors for highly monodisperse CQDs.

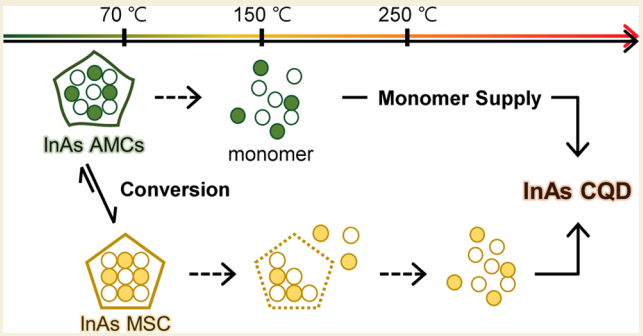

KEYWORDS: *indium arsenide, nanoclusters, magic-sized nanoclusters, colloidal quantum dots, synthetic precursors, atomic information*

INTRODUCTION

Since the discovery of colloidal quantum dots (CQDs), extensive efforts have been dedicated to their synthesis with high monodispersity.[1−6] The synthesis of CQDs involves the emergence of various intermediates, including nanoclusters, existing in thermodynamically local minimum energy states. Among these intermediates, atomically precise semiconductor nanoclusters, often referred to as magic-sized nanoclusters (MSC), are distinguished from other nanoclusters due to their distinct characterestics.[7] Being ultrasmall (∼10−100 core atoms and sizes below 2 nm), the physicochemical properties of nanoclusters and MSC are highly sensitive to their atomic structure, configuration, and surface; even a single atom or ligand difference can lead to significant variations in their physicochemical properties.[8−10]

Studies on the physicochemical properties and synthetic mechanisms of II−VI nanoclusters have been facilitated by a deeper understanding of the relationship between the structure and their properties, as well as nanocluster conversion. For example, the conversion kinetics of zinc and cadmium chalcogenide MSCs from amorphous-like nanoclusters were characterized by a continuous increase in absorbance at the first excitonic peak of MSC, suggesting first-order kinetics.[11−13] The discovery of the chemically reversible isomerization of cadmium sulfide (CdS) MSC from the reaction with alcohols was accounted for by subtle structural differences during intramolecular rearrangement.[10] However, in contrast to metallic nanoclusters, complete structural information is available for only a limited number of MSCs through single-crystal X-ray diffraction (XRD).[14] To overcome this limitation, the present studies employ various characterization techniques, including mass spectroscopy, X-ray scattering and absorption, nuclear magnetic resonance (NMR) spectroscopy, Fourier

Received: December 19, 2023
Revised: February 2, 2024
Accepted: February 6, 2024
Published: February 16, 2024

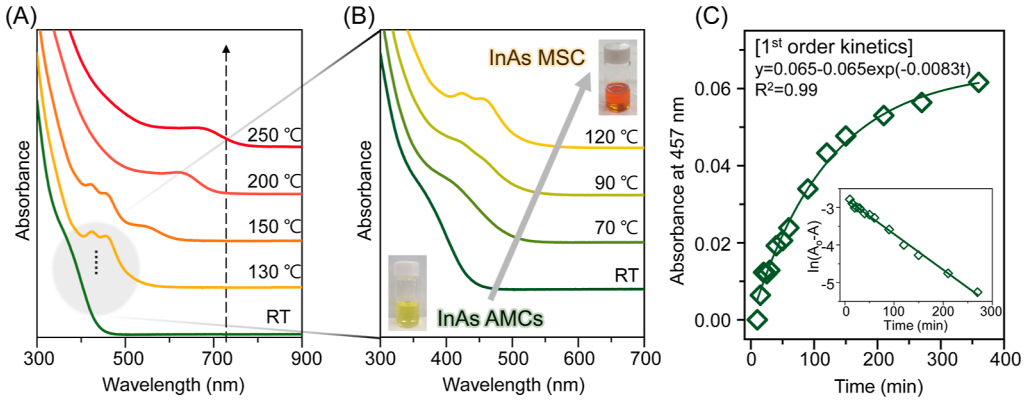

Figure 1. Early intermediate nanoclusters in the InAs CQD formation process. (A) Normalized absorption spectrum of aliquots taken after the injection of arsenic precursor into the indium oleate solution and heating from RT to 250 °C for the observation of the overall reaction pathway. (B) Normalized absorption spectrum from InAs AMCs (shown in green) to InAs MSC (shown in yellow) for the observation of the conversion process. (C) Kinetics of the conversion from InAs AMCs to MSC at 70 °C. After the injection of arsenic precursor into indium oleate solution, the absorption spectrum of aliquots was taken for up to 6 h. Well-fitted time-dependent absorbance values (denoted as A) at 457 nm (open diamonds, with the subtraction of the initial value) with the exponential plot mean that the conversion from InAs AMCs to MSC follows first-order kinetics (solid green line). Inset indicates the time-dependent $\ln(A_o - A)$. A_o represents the initial amount of InAs AMCs.

transform infrared (FTIR) spectroscopy, and density functional theory (DFT) calculations, to elucidate the physicochemical properties of nanoclusters.[15,16]

The commercialization of CQDs for optical devices,[17] such as light-emitting diodes and photodetectors, has driven intense research into III−V nanoclusters and MSCs. Among these, indium phosphide (InP) CQDs, used for generating visible-range photons, have been extensively studied and the complete structure of InP MSC has been reported.[18] Insights gained from understanding their structure and physicochemical properties have informed strategies for synthesizing high-quality InP CQDs.[8] More recently, indium arsenide (InAs) CQDs have emerged as promising materials for optoelectronic devices focused on infrared applications.[19,20] Unlike high-quality InP CQDs, the synthesis of monodisperse InAs CQDs has been challenging due to the highly reactive silyl-based arsine precursors. To address this challenge, the Jeong group employed InAs amorphous nanoclusters (AMCs), which likely serve as prenucleation- and liquid crystal-like nanoclusters, to facilitate the diffusion controlled growth of InAs CQDs.[5,21] Remarkably, these AMCs, stable at room temperature (RT), function as single-source precursors, enabling precise control over the size and size uniformity of InAs CQDs. Nevertheless, the role of InAs nanoclusters as synthetic precursors has remained unexplored.

Herein, we report the conversion of InAs MSC from AMCs, both appearing as reaction intermediates prior to nanocrystal formation, offering insights into the kinetics of this conversion process, which follows a first-order reaction. To gain a deeper understanding of this process, we isolated InAs nanoclusters from unreacted impurities using gel-permeation chromatography (GPC).[22] Through chemical and thermolysis reactions, purified InAs MSCs demonstrated greater stability when compared with InAs AMCs. Further structural characterization, employing techniques such as ^{1}H NMR spectroscopy, X-ray photoemission spectroscopy (XPS), and FTIR spectroscopy, revealed that the surface of InAs nanoclusters is exclusively bound with carboxylate ligands. Given their ultrasmall size, comprehensive structural characterization of InAs nanoclusters was conducted using synchrotron X-ray analysis, encompassing X-ray scattering and X-ray absorption spectroscopy. This analysis uncovered subtle structural differences between AMCs and MSCs, arising from distinct surface properties and structural disorders within InAs nanoclusters. These results suggest that the conversion from AMCs to MSCs involves a process that enhances stability by reducing the number of surface atoms and increasing the structural order. Importantly, at the elevated temperatures typically employed for the nucleation and growth of InAs CQDs, approximately 300 °C, both types of nanoclusters serve as precursors, providing a similar rate of monomer supply. This comprehensive investigation into the characterization of InAs nanoclusters promises to yield valuable insights into their structural attributes and offers strategies for the efficient application of nanoclusters as precursors.

RESULTS AND DISCUSSION

Formation of InAs Nanoclusters

In our exploration of the reaction pathways starting from the indium and arsenide precursor solution to InAs CQDs and incorporating various additive chemicals, we observed the emergence of InAs MSC[23,24] displaying two distinct peaks at the early stages of several reaction pathways. These peaks, located at 420 and 457 nm, are illustrated in Figures 1A and S1. Figure S1 demonstrates that the dioctylamine (DOA) and trioctylphosphine (TOP) are essential additives for the formation of InAs MSC. In line with previous reports,[25,26] DOA likely moderates the reactivity of the silylarsine precursor, tris(trimethylsilyl)arsine ($(TMS)_3As$), whereas TOP activates the reactivity of the indium precursor, oleate coordinated In precursors.[26] The addition of organophosphine induced the interaction between indium alkanoates and organophosphine, leading to the activation of the indium precursor via decarboxylation of the indium alkanoates and enhancing their solubility in hydrocarbon solvents.[27] Notably, Peng and co-workers reported the presence of InAs MSC prior to the formation of InAs CQD when organophosphines were used as additives in the reaction.[28] Similarly, the addition of organoamine induces the interaction between arsenide and organoamine, but the resulting complex hinders close approach to the indium precursor due to steric hindrance, ultimately reducing the reactivity of the arsenic precursor.[25,26] Therefore,

https://doi.org/10.1021/jacsau.3c00809
JACS Au 2024, 4, 1097−1106

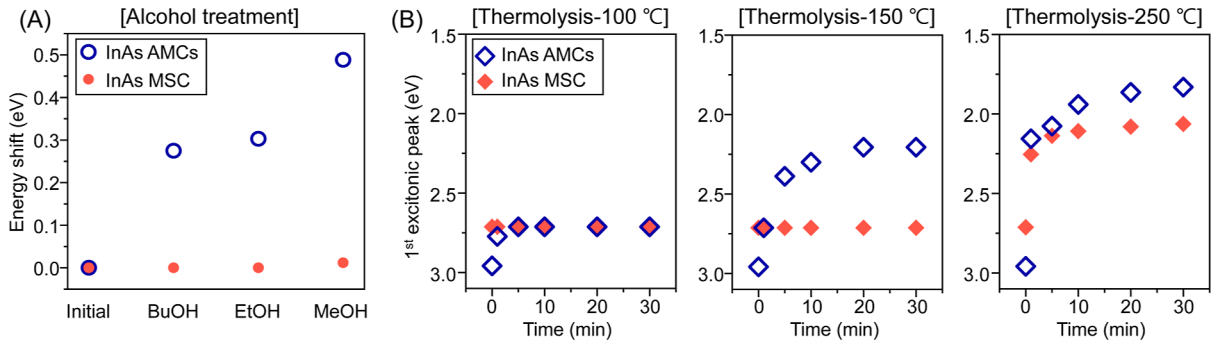

Figure 2. Chemical properties of InAs nanoclusters. (A) Excitonic energy shift before and after alcohol treatment in InAs nanoclusters. Purified InAs MSC (red circle) and InAs AMCs (blue open circle) dispersed in toluene were added to 0.5 μmol of alcohols (anhydrous butanol, ethanol, and methanol). The excitonic energy shift of InAs MSC was represented by the shift of 1st excitonic peak, and that of InAs AMCs was represented by the shift of an inflection point. (B) Time-dependent excitonic energy value of the 1st excitonic peak in the thermolysis experiment of InAs nanoclusters. Purified InAs MSC (red diamond) and InAs AMCs (blue open diamond) were injected in degassed *n*-hexadecane at 100/150/250 °C. After injection of nanoclusters, aliquots were taken for up to 30 min. The value at 0 min represents the excitonic energy value of the 1st excitonic peak of InAs MSC and an inflection point of InAs AMCs.

we propose that the balance of two precursor reactivities, wherein one reduces and the other increases the reactivity of the arsenic or indium precursor solution, respectively, plays a crucial role in the formation of InAs MSCs. We also noted that InAs nanoclusters synthesized with additives below 50 °C exhibited absorption at shorter wavelengths compared with cases where additives were not used (Figure S1).

In this study, we classify InAs AMCs as InAs nanoclusters displaying a shoulder-like absorption spectrum near 400 nm, which are synthesized immediately following the injection of the arsenic precursor with DOA at RT.[5] We hypothesize that these nanoclusters are stable, amorphous, or liquidlike in nature, as indicated by the persistent shoulder-like absorption feature observed up to 50 °C, as shown in Figures S1B and S2. A more comprehensive structural analysis of InAs AMCs will be presented later in this study.

Above 50 °C, the absorption spectrum gradually red-shifts and MSC emerges, accompanied by a color change from yellow to orange (Figure 1B). To investigate the conversion of the InAs MSC from AMCs, we monitored the kinetics at 70 °C, as depicted in the absorption spectrum shown in Figure S3. Our observations revealed that the conversion from InAs AMCs to InAs MSCs follows first-order kinetics, as described by the equations below

$$A = A_o - A_o \exp(-k_1 t) \quad (1)$$

$$\ln(A_o - A) = -k_1 t + C \quad (2)$$

Here, A represents the absorbance at 457 nm, k_1 is the rate constant, and C is a constant. The fitted line (green solid line) within the exponential function closely aligns with the experimental data ($R^2 = 0.99$), indicating that the rate constant is 8.3×10^{-3} min^{-1}. The inset of Figure 1C also shows a well-fitted result as a linear plot with eq 2 ($R^2 = 0.99$). As shown in Figure S4, the conversion process of InAs nanoclusters at different temperatures also follows the first-order process (80, 90, and 100 °C). Through the Arrhenius plot for the conversion kinetics, we estimated that the activation energy for the conversion process is 1.11 eV (107.31 kJ mol^{-1}, R^2 = 0.94). This result is similar to the behavior observed in the case of cadmium- and zinc-chalcogenide nanoclusters, where early stage nanoclusters transformed into MSCs with first-order kinetics, characterized by their similar composition and molecular mass,[11−13] which was interpreted as an intramolecular reorganization within the nanoclusters. Given the similarities in size between InAs MSCs and AMCs, as determined by scanning transmission electron microscopy (STEM) in Figure S5, and their first-order kinetics, we infer the existence of structural differences between InAs MSCs and AMCs.

For a more comprehensive characterization of the first-order conversion process and the resulting structure, we utilized InAs MSCs synthesized at 100 °C, a temperature at which they are rapidly formed without the formation of InAs CQDs, as depicted in Figure S6. Furthermore, purification of the InAs nanoclusters was performed using GPC to eliminate unreacted precursors.[22,29] In Figure S7, we demonstrate the removal of free oleic acid (OA) and 1-octadecene (ODE) by FTIR and ^{1}H NMR analysis.[30] In the FTIR spectra of purified nanoclusters, the broad −OH and sharp C═O peaks at 1705 cm^{-1}, typically associated with free OA, were not observed. Similarly, in the ^{1}H NMR spectra, the vinyl proton peaks of ODE at 5.0 ppm and free OA at 5.4−5.5 ppm disappeared, while the vinyl proton peak of bound oleate at 5.5 ppm remained in the purified nanoclusters. Importantly, after purification, the absorption spectrum of the InAs nanoclusters remained unchanged, as shown in Figure S8.

Chemical Properties of InAs Nanoclusters

After the purification of InAs nanoclusters, we thoroughly examined the reactivity of InAs nanoclusters in various chemical environments. First, we treated the purified InAs nanoclusters with alcohols and monitored changes in their absorption spectrum as an indicator of reactivity. As shown in Figures 2A and S9, treatment of butanol and ethanol did not result in any noticeable energy shift in the absorption spectrum of InAs MSC. However, when InAs AMCs were treated with butanol and ethanol, a discernible energy shift of 0.27 and 0.30 eV, respectively, was observed in their absorption spectra. Treatment with methanol induced a more significant energy shift of 0.49 eV in the absorption spectrum of InAs AMCs and a minor shift in InAs MSC. This difference in the excitonic energy shift strongly suggests that InAs MSCs exhibit greater stability when subjected to alcohol treatment compared to InAs AMCs. Interestingly, we also observed a correlation between the acidity of the alcohols used and the magnitude of the excitonic energy shift, hinting at a potential influence of

https://doi.org/10.1021/jacsau.3c00809
JACS Au 2024, 4, 1097−1106

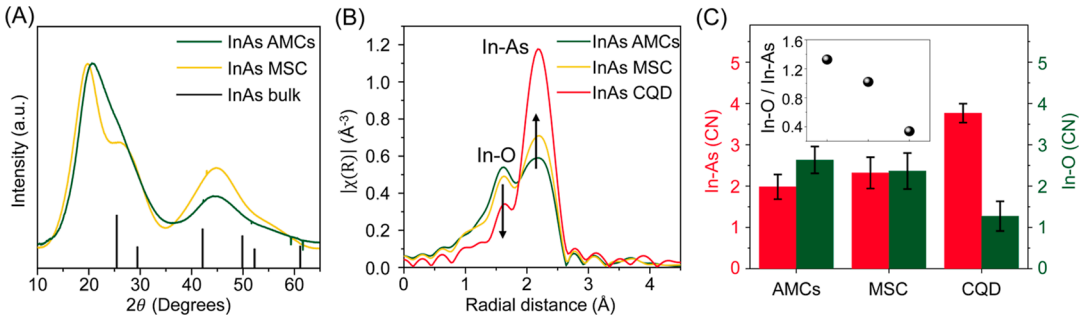

Figure 3. Structure difference in InAs nanoclusters and CQDs. (A) Synchrotron X-ray scattering spectra of InAs MSC (green), InAs AMCs (yellow), and InAs bulk (zinc blende) crystal's XRD line (black, ICDD PDF 00-015-0869) (B,C) Fourier transform magnitude of In K-edge extended X-ray absorption fine structure analysis (EXAFS) spectra and coordination number (CN) of InAs nanoclusters and CQD. Inset: In−O to In−As coordination number ratios of InAs nanoclusters and CQDs.

acidity in this phenomenon. However, the precise mechanism underlying the shift in excitonic peaks remains elusive. Prior research has demonstrated that methanol can accelerate the conversion of CdS MSCs from amorphous-like CdS nanoclusters and induce structural isomerization of CdS MSCs through ligand configuration changes.[9,10,13] Based on this, we propose two possible explanations for the excitonic peak shift: (1) Alcohols induce the conversion of InAs AMCs into another nanocluster or nanoparticle, or (2) they facilitate structural isomerization of InAs AMCs by altering the ligand configuration. Further investigation is needed to elucidate the origin of the excitonic peak shift in InAs AMCs and to understand the different behaviors of InAs MSC when exposed to alcohols compared to CdS MSCs.

Subsequently, we evaluated the thermal stability of InAs nanoclusters in various thermal environments. Purified nanoclusters were injected into degassed *n*-hexadecane at temperatures of 100, 150, and 250 °C. At 100 and 150 °C, as illustrated in Figures 2B and S10, InAs AMCs converted into MSCs and InAs CQDs, respectively, as previously discussed in Figure 1. Contrary to AMCs, MSCs remained stable without excitonic peak shifts at 100 and 150 °C. At 250 °C, right after injection, both types of InAs nanoclusters converted into InAs CQDs, exhibiting different growth characteristics. In the case of InAs MSCs shown in Figure S10, CQD grows more slowly than the case of InAs AMCs. This result indicated that the monomer supply rate of InAs MSC is slower than that of AMCs below 250 °C. We estimated that the difference in monomer supply rate originates from the difference in stability of InAs nanoclusters, which is consistent with a previous study.[8]

To explore the reaction tendencies of InAs nanoclusters under actual synthetic conditions, we performed thermolysis reactions using the crude solution of unpurified InAs nanoclusters at 250 and 300 °C. At 250 °C, as in Figures S11 and S12, similar trends in excitonic peak shifts were observed for both unpurified and purified nanoclusters, indicating that the monomer supply rate depends on the stability of InAs nanoclusters. Furthermore, at 300 °C, the first excitonic peaks of both nanoclusters exhibited comparable rate shifts. Based on these findings, we suggest that the monomer supply rates of the two nanoclusters will be similar at high temperatures of around 300 °C.

Structure Difference

To gain a deeper understanding of the conversion process and different chemical properties, we analyzed the ligand environment and structure of InAs nanoclusters. Through the ^{1}H NMR analysis in Figure S7, we identified the presence of the oleate ligands in InAs nanoclusters. On the other hand, DOA-related signals were not detected in both purified InAs nanoclusters, as confirmed through FTIR, XPS, and NMR analysis, as shown in Figure S13.[31,32] Specifically, these analyses did not reveal any detectable signals related to N−H stretches in the FTIR spectra, N 1s in their XPS spectra, or signals at 50 ppm in the ^{13}C NMR spectra. Additionally, the In 3d and As 3d XPS spectra of InAs nanoclusters showed no difference in binding energy or peak broadness, indicating similar ligand environments within these nanoclusters, as shown in Figure S14. Based on these results, we conclude that the surface of both InAs nanoclusters primarily consists of oleate ligands.

Before analyzing the structure of InAs nanoclusters, to elucidate the doublet optical transition of InAs MSC, we first constructed their atomic structure based on our observed physicochemical properties, employing DFT calculations. We hypothesize that the precise atomic structure of $In_{37}P_{20}$ MSC and InAs MSC is similar because the core structures of these two systems consist of the group III−V elements.[18] In the model construction, we adopted the core structure of $In_{37}P_{20}$ MSC for the InAs core, with the phosphorus (P) atom replaced by an As atom. Additionally, we aimed to match the absorption spectrum's peak positions with experimental data. As for the InAs MSC model in Figure S15, we developed a new model system with an $In_{39}As_{22}$ core structure, preserving C_2 symmetry. By comparing ab initio simulated and measured spectroscopy data (including optical transition, X-ray scattering, and inductively coupled plasma mass spectrometry in Figure S15 and Table S1, respectively), we validated our model system of InAs MSC.[33−35]

For the construction of the InAs AMCs model, we considered the first-order kinetics and the size distribution of STEM images in Figure S5, suggesting that InAs AMCs and MSCs share similar size and composition in their atomic structure. We explored the atomic structures of InAs AMCs by rearranging the surface atoms of InAs MSC with a disruption of C_2 symmetry, as shown in Figure S16.

Leveraging our model systems for InAs AMCs and MSCs, we propose an interpretation to elucidate the fundamental distinction in optical transitions between these two systems. The most critical difference is the presence or absence of C_2 symmetry. In Figure S17, the HOMO and LUMO of InAs MSC with C_2 symmetry exhibit widespread dispersion in the atomic structure. This large overlap of molecular orbitals

https://doi.org/10.1021/jacsau.3c00809
JACS Au 2024, 4, 1097−1106

Scheme 1. Schematic Illustration of the Conversion and Monomer Supply Process of InAs Nanoclusters; (A) InAs AMCs Convert into Stable MSC by Reducing the Number of Surface Atoms and Crystal Disorder and (B) Monomer Supply Rate of InAs AMCs is Faster than That of MSC at Temperatures below 250 °C; at Around 300 °C, Monomer Supply Rates of the Two Nanoclusters Become Similar[a]

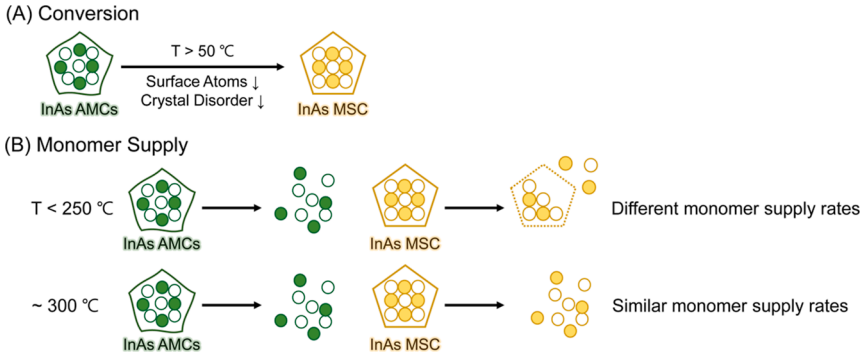

[a]White and color circles represent indium and arsenic atoms, respectively.

strongly induces the HOMO−LUMO electronic transition, which contributes to the formation of two peaks in the absorption spectrum for InAs MSC. In the other case, the disruption of C_2 symmetry induces the separation and localization of the HOMO and LUMO in InAs AMCs. As a result, the small overlap of molecular orbitals makes the first HOMO−LUMO electronic transition weak and more higher energy transitions strong, which indicates the relatively blue-shifted shoulder peak of the InAs AMCs absorption spectrum.

To gain further insights into the structure, we analyzed the structure of InAs nanoclusters through synchrotron X-ray scattering, acknowledging that both nanoclusters exhibited similar broad peaks as in Figures 3A, S18, and S19. In the case of nanoclusters, scattering peaks become notably broad, which is known as Scherrer broadening.[36] In situations where the ordering of lattice coherence diminishes significantly, these broad peaks do not provide a meaningful explanation for bulk crystal XRD line peaks.[8,23] Figure 3A also shows the presence of broad peaks around 20, 27, and 44° in both AMCs and MSCs. In order to obtain the ratio of each peak in the scattering spectra, we normalized the data with the main peak at 20°, originating from the surface phase and organic ligands.[37] The coherence peaks at approximately 27 and 44° signify that AMCs and MSCs share a similar structural aspect. Nevertheless, a notable distinction lies in the resolution of coherence peaks, with those of MSCs being more pronounced. This difference implies that InAs AMCs possess a greater number of surface atoms and fewer core atoms, a conclusion that aligns with thermogravimetric (TGA) analysis as detailed in Table S2.

For a more comprehensive understanding of the structural differences between InAs AMCs and MSCs, we conducted extended X-ray absorption fine structure (EXAFS) analysis, a technique that offers insights into local bonding and coordination environments. The EXAFS spectra of the In and As K absorption edges are presented in Figures 3B and S20, respectively. The EXAFS fitting results are summarized in Table S3. We used an InAs CQD sample as a reference, which has a more pronounced In−As EXAFS peak with a low surface-to-volume ratio compared to that of nanocluster samples.

Figure 3B shows two peaks in the In K-edge EXAFS spectra, identified as In−As and In−O bonds, respectively. The increase and decrease of the In−As and In−O peaks, respectively, originate from the change in coordination number (CN) of each bonding shell.[38] We summarize the CNs and the ratio of the In−As and In−O bonding shells in Figure 3C and inset. The InAs CQDs have a low ratio of In−O to In−As CNs, consistent with the low surface-to-volume ratio. In contrast, InAs AMCs and MSC nanoclusters demonstrate a substantial ratio of In−O to In−As CNs, indicative of a higher proportion of surface atoms. However, there are also subtle differences in the CNs and the CN ratios between InAs nanoclusters. To explain these differences, we calculated the CN of In−As from our model structure in Table S4. The In−As CN values of 1.98 and 2.32, obtained from EXAFS fitting of InAs AMCs and MSC, respectively, are in good agreement with the calculated CN values of 2.00 and 2.26. The decrease in the ratio between In−O and In−As CNs, shown in the inset of Figure 3C, indicates that InAs MSC have fewer surface atoms compared to InAs AMCs, which is consistent with the interpretations based on scattering analysis. The nanocluster and CQD show similar bond lengths of In−As and In−O of 2.60−2.62 and 2.20−2.23 Å, respectively, which verifies that the bond distance is not sensitive to the increase in sample size and the conversion of nanoclusters.

Considering our comprehensive structural characterizations of InAs AMCs and MSC, we propose that the reduction of the number of surface In atoms and increase of the crystal order within InAs AMCs significantly contribute to the conversion into InAs MSC, as shown in Scheme 1A.

InAs Nanoclusters as Synthetic Precursors

Previous studies on InP nanoclusters showed that their thermal stabilities vary depending on the surface ligands, which results in the variation of monomer supply capacity.[8] For example, phosphonate-terminated InP MSC was unable to efficiently provide monomers because they are overly stable at a high temperature. In contrast, carboxylate-terminated InP MSC served as an effective single-source precursor for the synthesis of In CQDs. As we discussed in our thermolysis experiments, both InAs nanoclusters exhibited different monomer supply rates below 250 °C, reflecting the difference in their stability. However, as temperatures increased beyond 250 °C, both types of nanoclusters displayed comparable monomer supply rates. These findings regarding the monomer supply rates at varying temperatures are summarized in Scheme 1B.

To clarify the temperature-dependent monomer supply rate of InAs nanoclusters for InAs CQD growth, we monitored the

https://doi.org/10.1021/jacsau.3c00809
JACS Au 2024, 4, 1097−1106

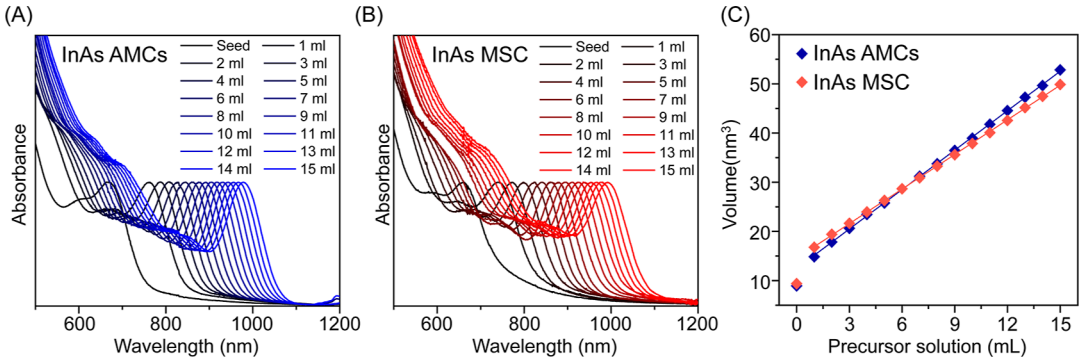

Figure 4. InAs nanoclusters as synthetic precursors. Normalized absorption spectrum of aliquots obtained from crude solution using a continuous injection rate of 6 mL/h for (A) InAs AMCs and (B) MSC precursor solution at 300 °C. Legends indicate the volume of the injected precursor solution. (C) CQD volumes depending on the injected precursor solution (colored line + symbol), estimated from (A,B) using the Brus equation.

absorption spectrum by hot injection of the InAs nanoclusters into InAs seeds at 250 and 300 °C, as shown in Figure S21. We observed that InAs MSC provides slower monomer supply rates compared to InAs AMCs at 250 °C for InAs CQD growth; however, at 300 °C, both types of nanoclusters exhibited similar monomer supply rates, which is consistent with thermolysis experiments (Figure 3B).

Because of the highly covalent nature of III−Vs, the elevated temperature, typically around 300 °C, is essential for the synthesis of high-crystalline and monodisperse III−V CQD.[39,40] Our research group employed a continuous injection method,[41] involving the introduction of InAs AMCs into InAs CQD "seeds", in order to separate nucleation and growth. This method has consistently resulted in the uniform growth of InAs CQDs, as previously demonstrated.[5] The underlying principle of this approach lies in maintaining a monomer supply rate from InAs AMCs that surpasses the rate of precursor injection, thus ensuring that the monomer concentration is consistently controlled by the precursor injection rate. To investigate the functionality as synthetic precursors of InAs AMCs and MSC for the growth of InAs CQDs via the continuous injection method, we meticulously tracked the CQD growth through the absorption spectrum by continuous injection of the InAs nanoclusters into InAs seeds at 300 °C, as shown in Figure 4. Detailed experimental methods are described in the experimental section. As shown in Figure 4A,B, the first excitonic peak undergoes a gradual red shift, accompanied by an enhancement in the size uniformity. To facilitate precise comparisons of growth extents, we applied the Brus equation[42] to convert each first excitonic peak in the absorption spectrum (Figure 4A,B) into the volume of InAs CQDs. The results in Figure 4C illustrate a comparable growth rate, aligning well with a linear plot. These results indicate that the monomer supply rate of InAs MSCs is sufficiently robust to support the growth of monodisperse InAs CQDs at 300 °C.

CONCLUSIONS

In summary, our exploration of the chemical reactions starting from InAs AMCs has unveiled a key insight into their conversion of InAs AMCs into MSC, which is characterized by first-order kinetics. By monitoring the shifts in the optical transition during both alcohol treatment and thermolysis reactions, we have directly ascertained that InAs MSCs exhibit a notably higher degree of stability than AMCs. Additionally, we have elucidated how the stability of InAs nanoclusters significantly influences their respective monomer supply rates. Through the structure analysis, we confirmed that their surfaces are predominantly coordinated with carboxylate ligands. To gain a deeper understanding of their structures, we employed simulations to construct model structures and conducted measurements using synchrotron X-ray scattering and absorption techniques, thereby elucidating their physicochemical properties. Our findings reveal that InAs AMCs and MSC have not only the shared structural characteristics but are also different in their surface composition and degree of crystal disorder. These results suggest that processes involving the reduction of surface atoms and structural disorder play a pivotal role in driving the conversion of InAs AMCs into MSC, ultimately enhancing their stability. Furthermore, our research has demonstrated that both types of InAs nanoclusters proficiently supply monomers for the growth of high-quality InAs CQDs under elevated temperatures. Together, our studies serve as a stepping stone for further investigations into the structural attributes of III−V nanoclusters and the development of innovative synthetic methodologies aimed at producing high-quality III−V CQDs.

METHODS

Chemicals and Materials

Indium(III) acetate (InOAc, UNIAM, 99.99%), oleic acid (OA, UNIAM, 99%), 1-octadecene (ODE, UNIAM, 99.99%), dioctylamine (DOA, Aldrich, 97%), tris(trimethylsilyl)arsine ($(TMS)_3As$, JSI silicon, 99%), trioctylphosphine (TOP, UNIAM), and *n*-hexadecane (Alfa Aesar, 99%) were used as purchased without any further purification. All solvents, including anhydrous methanol, butanol, ethanol, hexane, toluene, and tetrachlorethylene (TCE), were purchased from Sigma-Aldrich Chemical Co. Bio Beads S-X1 GPC medium was purchased from Bio-Rad Laboratories, Inc. Deuterated toluene was purchased from DEUTERO.

Synthesis and Purification of InAs Nanoclusters

Both InAs nanoclusters were prepared by using the same In and As precursor solutions. For the In precursor solution, 1 mmol InOAc and 3 mmol OA were degassed in 5 mL of ODE at 100 °C for 2 h. For the As precursor solution, 0.5 mmol of TMS_3As was mixed with 1.5 mmol of DOA and 1 mL of ODE in a glovebox and annealed at 60 °C. For InAs AMCs synthesis, As precursor solution was rapidly injected into the degassed In precursor solution at RT under nitrogen conditions and reacted for 10 min. For the InAs MSC, In and As precursor solutions were prepared using the same method and reacted at 100 °C for 90 min under nitrogen conditions.

After synthesis, purification of InAs nanoclusters was performed using a GPC column in a glovebox.[43] GPC column was packed at a height of ∼30 cm with bio beads swollen in anhydrous toluene. 1.5

https://doi.org/10.1021/jacsau.3c00809
JACS Au 2024, 4, 1097−1106

mL of crude nanocluster sample dispersed in the ODE was injected into the GPC column, and approximately 10 mL of purified sample was collected. Anhydrous toluene was used to rinse the column after the purification. The purified samples were confirmed to be free of impurities (ODE, free oleic acid, etc.) through ^{1}H NMR spectroscopy and FTIR spectroscopy.

Monitoring the Overall InAs Nanocluster Reactions

For heating experiments using DOA, In and As precursor solutions were prepared using the same method as described in the previous section. In the case of the heating experiment without additives, DOA was not used in the preparation of the As precursor solutions. In the case of the heating experiment using TOP, TOP was injected into a degassed In precursor solution at RT. After the As precursor solution was rapidly injected into the In precursor, the solution reacted at RT for 10 min. After that, the solution was then heated from RT to 300 °C at a rate of 1 °C/min. Aliquots were taken RT and every 10 °C.

For conversion from InAs AMCs to InAs MSC experiments, In and As precursor solutions were prepared using the same method as described in the previous section and reacted at 70 °C for 6 h under nitrogen conditions.

Chemical Properties of InAs Nanoclusters

For alcohol treatment experiments, 2 mg of purified InAs nanoclusters were treated with 0.5 μmol of each alcohol (anhydrous butanol, ethanol, and methanol) under a nitrogen condition. To ensure a complete reaction, absorption spectra were obtained after 1 h.

For thermolysis experiments using purified nanoclusters, 10 mg of purified nanoclusters dispersed in 1 mL of *n*-hexadecane was prepared. The prepared nanoclusters were injected into *n*-hexadecane under nitrogen conditions at 100/150/250 °C, respectively. Aliquots were taken RT for up to 30 min. All the *n*-hexadecane used in these experiments was degassed at 90 °C for 2 h under vacuum.

For thermolysis experiments using crude nanoclusters, 0.5 mL of crude nanoclusters were injected into degassed ODE under nitrogen conditions at 250/300 °C, respectively. Aliquots were taken RT and up to 30 min.

Continuous Injection and Hot Injection of InAs Nanoclusters

In and As precursor solutions were prepared using the same method as described in the previous section for the synthesis of InAs seeds. For the synthesis of InAs seed, As solution was rapidly injected into In solution at 300 °C under nitrogen conditions. After that, the InAs nanocluster solutions were continuously injected into the seed solution using a syringe pump at a rate of 0.1 mL/min, respectively. In the hot injection method, the InAs nanocluster solutions (2 mL) were rapidly injected into the seed solution at 250 and 300 °C.

Characterization

Absorption spectra of InAs nanoclusters were obtained using UV3600(Shimadzu). STEM images of InAs nanoclusters were obtained using JEM-ARM200F(JEOL). FTIR spectra were collected using an is50 FTIR spectrometer (Thermo Fisher Scientific). The FTIR sample was deposited on the Si/Cr/Au substrate. ^{1}H and ^{13}C NMR spectra were measured using 500 MHz NMR (Bruker) with 32 scans at the Chiral Material Core Facility Center of Sungkyunkwan University. All samples were prepared in deuterated toluene (d_8-toluene). Inductively coupled plasma mass spectrometry (ICP−MS) was measured using 7900 ICP−MS (Agilent) with microwave pretreatment. TGA was measured using an STA7200RV from RT to 600 °C with nitrogen flow.

Synchrotron XPS, scattering, and absorption measurements were conducted at the PLS-II 10A2, 6D, and 10C beamlines of Pohang Accelerator Laboratory (PAL) in South Korea, respectively. For the XPS measurement, films were prepared on a Si substrate coated with a Cr/Au (10/100 nm) layer. Binding energies were calibrated using the C 1s core level (284.8 eV). For X-ray scattering measurements, the X-rays were monochromated using Si(111) double crystals, resulting in 18.986 keV photons. The scattering signals were recorded with a 2D CCD detector (MX225-Hs, Rayonix), and diffraction angles were calibrated by a precalibrated LaB_6 (NIST SRM 660C LaB_6). The X-ray irradiation time was 10−100 s, dependent on the saturation level of the detector. The sample-to-detector distance was about 240 mm. Before measuring scattering, blank capillaries were measured in the desired scattering ranges to exclude the background signal. InAs nanoclusters were mounted in the measured capillaries (1.5 mm diameter). For XAS, the X-rays were monochromated using Si(111) and Si(311). The intensity of source, fluorescent, and transmitted X-rays are detected by the first ionization chamber, Ge array, and second ionization chamber detectors, respectively. InAs nanoclusters were mounted on Scotch tape and overlapped several times in a nitrogen-filled glovebox. The XAS measurements were carried out at the In and As K-edges using both transmission and fluorescence modes. Background subtraction and normalization were performed using ATHENA software. For fitting the In and As K-edge EXAFS spectra, we used In−As and In−O scattering paths covering *k*-space ranging from 3.0 to 12.0 Å^{-1}, *R*-space spanning from 1.5 to 3.0 Å, and R_{bkg} of 1.0 Å. The best fits were achieved when the In−As and In−O paths were used. All scattering paths were generated using the FEFF6 calculation, and S_0^2 values for In and As were obtained by reference values of 0.82 and 0.839, respectively.[20,44] Coordination number (CN), bond length (*R*), and mean square relative displacement (σ^2) were treated as variables.

Simulation

DFT total-energy calculations were performed using the generalized gradient approximation (GGA-PBE[45]) and the projector-augmented wave (PAW) method,[46] as implemented in the Vienna Ab-initio Simulation Package.[47,48] We used an energy cutoff of 400 eV for the plane wave part of the wave function. The van der Waals interaction was included using the PBE-D3 method of Grimme.[49] To obtain the optimized geometries of InAs nanoclusters, we fully relaxed all atoms in the clusters until the residual forces were below 0.05 eV/Å.

The HSE06 range-separated hybrid functional[50,51] was used to obtain the linear-response time-dependent DFT (TDDFT) absorption spectra[52] of the identified InAs nanoclusters, as implemented in the Gaussian electronic structure package.[53] PBE-relaxed structures were used to reduce computational costs. For the TDDFT calculations, the LANL2DZ basis set was used to describe In and As atomic orbitals, and the 6-31G(d) basis set was used for other elements. Linear response TDDFT was used to compute the excitation energies and corresponding oscillator strengths of the first 10 electronic transitions.

The scattering intensity in simulated X-ray scattering patterns was obtained using the Debye formula[54]

$$I(Q) = f^{DW} \sum_{i,j} \frac{f_i(Q) f_j(Q) \sin(Qr_{ij})}{Qr_{ij}}$$

where r_{ij} is the interatomic distance between atoms *i* and *j*, and $f_i(Q)$ is the atomic scattering factor of atom *i* at the scattering vector length *Q*. The tabulated values of $f_i(Q)$ were taken from reference values[55] and $Q = 4\pi \sin(\theta)/\lambda$ for the scattering angle 2_θ and incident wavelength λ. The Debye−Waller factor, $f^{DW} = \exp\left(-\frac{BQ^2}{2}\right)$, with $B = 0.04$ Å^2 was introduced to account for the thermal motion of atoms.

■ ASSOCIATED CONTENT

Supporting Information

The Supporting Information is available free of charge at https://pubs.acs.org/doi/10.1021/jacsau.3c00809.

The Supporting Information is available free of charge on the ACS Publications Web site. Absorption spectrum taken aliquots during growth of InAs quantum dots during heat up, hot injection, and continuous injection methods, absorption spectrum of crude and purified InAs nanoclusters, absorption spectrum and kinetics of InAs nanocluster conversion process, absorption spec-

https://doi.org/10.1021/jacsau.3c00809
JACS Au 2024, 4, 1097−1106

trum of chemical treatment with alcohols and thermolysis experiments, image of GPC column setup, STEM image, ^{1}H NMR spectra, ICP−MS data, TGA analysis, total scattering spectra of InAs nanoclusters, XPS spectra, ^{13}C NMR, and FTIR spectra of InAs nanoclusters and other compounds, EXAFS spectra of InAs nanoclusters and InAs CQD, simulation models, and absorption simulation of the nanocluster models (PDF)

AUTHOR INFORMATION

Corresponding Author

Sohee Jeong − *Department of Energy Science (DOES) and Center for Artificial Atoms, Sungkyunkwan University (SKKU), Suwon, Gyeonggi-do 16419, South Korea; Sungkyunkwan Institute of Energy Science and Technology (SIEST), Sungkyunkwan University (SKKU), Suwon, Gyeonggi-do 16419, South Korea;* orcid.org/0000-0002-9863-1374; Email: s.jeong@skku.edu

Authors

Jibin Shin − *Department of Energy Science (DOES) and Center for Artificial Atoms, Sungkyunkwan University (SKKU), Suwon, Gyeonggi-do 16419, South Korea*

Mahnmin Choi − *Department of Energy Science (DOES) and Center for Artificial Atoms, Sungkyunkwan University (SKKU), Suwon, Gyeonggi-do 16419, South Korea*

Doeun Shim − *Department of Physics and Chemistry, DGIST, Daegu 42988, South Korea*

Tyler Joe Ziehl − *Department of Chemistry, Dalhousie University, Halifax NSB3H 4R2, Canada*

Seongmin Park − *Department of Energy Science (DOES) and Center for Artificial Atoms, Sungkyunkwan University (SKKU), Suwon, Gyeonggi-do 16419, South Korea*

Eunhye Cho − *Department of Energy Science (DOES) and Center for Artificial Atoms, Sungkyunkwan University (SKKU), Suwon, Gyeonggi-do 16419, South Korea*

Peng Zhang − *Department of Chemistry, Dalhousie University, Halifax NSB3H 4R2, Canada;* orcid.org/0000-0003-3603-0175

Hangil Lee − *Department of Chemistry, Sookmyung Women's University, Seoul 04310, South Korea;* orcid.org/0000-0002-0657-5660

Joongoo Kang − *Department of Physics and Chemistry, DGIST, Daegu 42988, South Korea;* orcid.org/0000-0001-7802-3235

Complete contact information is available at: https://pubs.acs.org/10.1021/jacsau.3c00809

Author Contributions

#J.S. and M.C. contributed equally. CRediT: **Jibin Shin** data curation, formal analysis, investigation, methodology, validation, writing-original draft; **Mahnmin Choi** data curation, formal analysis, investigation, methodology, writing-original draft; **Doeun Shim** data curation, formal analysis, methodology, software; **Tyler Joe Ziehl** formal analysis, methodology; **Seongmin Park** data curation, methodology; **Eunhye Cho** data curation; **Peng Zhang** investigation, methodology, supervision, validation, writing-review & editing; **Hangil Lee** data curation, formal analysis; **Joongoo Kang** conceptualization, investigation, methodology, supervision, validation, writing-review & editing; **Sohee Jeong** conceptualization, investigation, project administration, supervision, writing-review & editing.

Notes

The authors declare no competing financial interest.

ACKNOWLEDGMENTS

This research was supported by the Creative Materials Discovery Program through the National Research Foundation (NRF) of Korea (NRF-2019M3D1A1078299), an NRF grant funded by the MSIT (NRF-2022R1A2C2091486), and Grant RS-2022-00144108 funded by the Ministry of Trade, Industry and Energy of the Korean government. P.Z. acknowledges NSERC Canada for funding, and T.J.Z. thanks the financial support of an NSGS scholarship.

REFERENCES

(1) Murray, C. B.; Norris, D. J.; Bawendi, M. G. Synthesis and characterization of nearly monodisperse CdE (E = sulfur, selenium, tellurium) semiconductor nanocrystallites. *J. Am. Chem. Soc.* **1993**, *115*, 8706−8715.

(2) Murray, C. B.; Kagan, C. R.; Bawendi, M. G. synthesis and characterization of monodisperse nanocrystals and close-packed nanocrystal assemblies. *Annu. Rev. Mater. Sci.* **2000**, *30*, 545−610.

(3) Tamang, S.; Lincheneau, C.; Hermans, Y.; Jeong, S.; Reiss, P. Chemistry of InP Nanocrystal Syntheses. *Chem. Mater.* **2016**, *28*, 2491−2506.

(4) Cumberland, S. L.; Hanif, K. M.; Javier, A.; Khitrov, G. A.; Strouse, G. F.; Woessner, S. M.; Yun, C. S. Inorganic Clusters as Single-Source Precursors for Preparation of CdSe, ZnSe, and CdSe/ZnS Nanomaterials. *Chem. Mater.* **2002**, *14*, 1576−1584.

(5) Kim, T.; Park, S.; Jeong, S. Diffusion dynamics controlled colloidal synthesis of Highly monodisperse InAs nanocrystals. *Nat. Commun.* **2021**, *12*, 3013.

(6) Li, L.; Zhang, J.; Zhang, M.; Rowell, N.; Zhang, C.; Wang, S.; Lu, J.; Fan, H.; Huang, W.; Chen, X.; Yu, K. Fragmentation of Magic-Size Cluster Precursor Compounds into Ultrasmall CdS Quantum Dots with Enhanced Particle Yield at Low Temperatures. *Angew. Chem.* **2020**, *132*, 12111−12119.

(7) Harrell, S. M.; McBride, J. R.; Rosenthal, S. J. Synthesis of Ultrasmall and Magic-Sized CdSe Nanocrystals. *Chem. Mater.* **2013**, *25*, 1199−1210.

(8) Gary, D. C.; Terban, M. W.; Billinge, S. J. L.; Cossairt, B. M. Two-Step Nucleation and Growth of InP Quantum Dots via Magic-Sized Cluster Intermediates. *Chem. Mater.* **2015**, *27*, 1432−1441.

(9) Nevers, D. R.; Williamson, C. B.; Hanrath, T.; Robinson, R. D. Surface chemistry of cadmium sulfide magic-sized clusters: a window into ligand-nanoparticle interactions. *Chem. Commun.* **2017**, *53*, 2866−2869.

(10) Williamson, C. B.; Nevers, D. R.; Nelson, A.; Hadar, I.; Banin, U.; Hanrath, T.; Robinson, R. D. Chemically reversible isomerization of inorganic clusters. *Science* **2019**, *363*, 731−735.

(11) Liu, S.; Yu, Q.; Zhang, C.; Zhang, M.; Rowell, N.; Fan, H.; Huang, W.; Yu, K.; Liang, B. Transformation of ZnS Precursor Compounds to Magic-Size Clusters Exhibiting Optical Absorption Peaking at 269 nm. *J. Phys. Chem. Lett.* **2020**, *11*, 75−82.

(12) Luan, C.; Gökçinar, Ö. Ö.; Rowell, N.; Kreouzis, T.; Han, S.; Zhang, M.; Fan, H.; Yu, K. Evolution of Two Types of CdTe Magic-Size Clusters from a Single Induction Period Sample. *J. Phys. Chem. Lett.* **2018**, *9*, 5288−5295.

(13) Zhu, T.; Zhang, B.; Zhang, J.; Lu, J.; Fan, H.; Rowell, N.; Ripmeester, J. A.; Han, S.; Yu, K. Two-Step Nucleation of CdS Magic-Size Nanocluster MSC-311. *Chem. Mater.* **2017**, *29*, 5727−5735.

(14) Bootharaju, M. S.; Baek, W.; Deng, G.; Singh, K.; Voznyy, O.; Zheng, N.; Hyeon, T. Structure of a subnanometer-sized semiconductor $Cd_{14}Se_{13}$ cluster. *Chem* **2022**, *8*, 2978−2989.

(15) Shin, J.; Choi, M.; Kim, M.; Jeong, S. Semiconductor clusters: Synthetic precursors for colloidal quantum dots. *Front. Nanotechnol.* **2022**, *4*, 1069178.
(16) Kwon, Y.; Kim, S. Indium phosphide magic-sized clusters: chemistry and applications. *NPG Asia Mater.* **2021**, *13*, 37.
(17) Kim, T.; Shin, D.; Kim, M.; Kim, H.; Cho, E.; Choi, M.; Kim, J.; Jang, E.; Jeong, S. Development of Group III-V Colloidal Quantum Dots for Optoelectronic Applications. *ACS Energy Lett.* **2023**, *8*, 447−456.
(18) Gary, D. C.; Flowers, S. E.; Kaminsky, W.; Petrone, A.; Li, X.; Cossairt, B. M. Single-Crystal and Electronic Structure of a 1.3 nm Indium Phosphide Nanocluster. *J. Am. Chem. Soc.* **2016**, *138*, 1510−1513.
(19) Park, Y.; Bae, S. Y.; Kim, T.; Park, S.; Oh, J. T.; Shin, D.; Choi, M.; Kim, H.; Kim, B.; Lee, D. C.; Song, J. H.; Choi, H.; Jeong, S.; Kim, Y. Charge-Selective, Narrow-Gap Indium Arsenide Quantum Dot Layer for Highly Stable and Efficient Organic Photovoltaics. *Adv. Energy Mater.* **2022**, *12*, 2104018.
(20) Yoon, J. I.; Kim, H.; Kim, M.; Cho, H.; Kwon, Y. A.; Choi, M.; Park, S.; Kim, T.; Lee, S.; Jo, H.; Kim, B. S.; Cho, J. H.; Park, J. S.; Jeong, S.; Kang, M. S. P- and N-Type InAs Nanocrystals with innately controlled semiconductor polarity. *Sci. Adv.* **2023**, *9*, No. eadj8276.
(21) Tamang, S.; Lee, S.; Choi, H.; Jeong, S. Tuning Size and Size Distribution of Colloidal InAs Nanocrystals via Continuous Supply of Prenucleation Clusters on Nanocrystal Seeds. *Chem. Mater.* **2016**, *28*, 8119−8122.
(22) Shen, Y.; Gee, M. Y.; Tan, R.; Pellechia, P. J.; Greytak, A. B. Purification of Quantum Dots by Gel Permeation Chromatography and the Effect of Excess Ligands on Shell Growth and Ligand Exchange. *Chem. Mater.* **2013**, *25*, 2838−2848.
(23) Ning, J.; Banin, U. Magic Size InP and InAs Clusters: Synthesis, Characterization and Shell Growth. *Chem. Commun.* **2017**, *53*, 2626−2629.
(24) Xie, R.; Peng, X. Synthetic Scheme for High-Quality InAs Nanocrystals Based on Self-Focusing and One-Pot Synthesis of InAs-Based Core-Shell Nanocrystals. *Angew. Chem., Int. Ed.* **2008**, *47*, 7677−7680.
(25) Song, J. H.; Choi, H.; Pham, H. T.; Jeong, S. Energy level tuned indium arsenide colloidal quantum dot films for efficient photovoltaics. *Nat. Commun.* **2018**, *9*, 4267.
(26) Allen, P. M.; Walker, B. J.; Bawendi, M. G. Mechanistic Insights into the Formation of InP Quantum Dots. *Angew. Chem., Int. Ed.* **2010**, *49*, 760−762.
(27) Li, Y.; Hou, X.; Shen, Y.; Dai, N.; Peng, X. Tuning the Reactivity of Indium Alkanoates by Tertiary Organophosphines for the Synthesis of Indium-Based Quantum Dots. *Chem. Mater.* **2021**, *33*, 9348−9356.
(28) Xu, Z.; Li, Y.; Li, J.; Pu, C.; Zhou, J.; Lv, L.; Peng, X. Formation of Size-Tunable and Nearly Monodisperse InP Nanocrystals: Chemical Reactions and Controlled Synthesis. *Chem. Mater.* **2019**, *31*, 5331−5341.
(29) Kwon, Y.; Oh, J.; Lee, E.; Lee, S. H.; Agnes, A.; Bang, G.; Kim, J.; Kim, D.; Kim, S. Evolution from unimolecular to colloidal-quantum-dot-like character in chlorine or zinc Incorporated InP magic size clusters. *Nat. Commun.* **2020**, *11*, 3127.
(30) Choi, M.; Kim, M.; Lee, Y.; Kim, T.; Kim, J. H.; Shin, D.; Kim, J. W.; Kim, Y. H.; Jeong, S. Tailored Band Edge Positions by Fractional Ligand Replacement of Nonconductive Colloidal Quantum Dot Films. *J. Phys. Chem. C* **2023**, *127*, 4825−4832.
(31) Zhou, Y.; Jiang, R.; Wang, Y.; Rohrs, H. W.; Rath, N. P.; Buhro, W. E. Isolation of Amine Derivatives of $(ZnSe)_{34}$ and $(CdTe)_{34}$. Spectroscopic Comparisons of the $(II\text{-}VI)_{13}$ and $(II\text{-}VI)_{34}$ Magic-Size Nanoclusters. *Inorg. Chem.* **2019**, *58*, 1815−1825.
(32) Lawrence, K.; Watkins, J. D.; James, T. D.; Taylor, J. E.; Bull, S. D.; Nelson, G. W.; Foord, J. S.; Long, Y. T.; Marken, F. Dioctylamine-Sulfonamide-Modified Carbon Nanoparticles as High Surface Area Substrates for Coenzyme Q10-Lipid Electrochemistry. *Electroanalysis* **2012**, *24*, 1003−1010.
(33) Nguyen, K. A.; Pachter, R.; Day, P. N. Systematic Study of the Properties of CdS Clusters with Carboxylate Ligands Using a Deep Neural Network Potential Developed with Data from Density Functional Theory Calculations. *J. Phys. Chem. A* **2020**, *124*, 10472−10481.
(34) Shim, D.; Lee, J.; Kang, J. Multiscale Isomerization of Magic-Sized Inorganic Clusters Chemically Driven by Atomic-Bond Exchanges. *Chem. Mater.* **2022**, *34*, 9527−9535.
(35) Shim, D.; Kang, J. Enhanced Reactivity of Magic-Sized Inorganic Clusters by Engineering the Surface Ligand Networks. *Chem. Mater.* **2023**, *35*, 700−708.
(36) Thomas, G. S.; Kamath, P. V. Line broadening in the PXRD patterns of layered hydroxides: The relative effects of crystallite size and structural disorder. *J. Chem. Sci.* **2006**, *118*, 127−133.
(37) Calvin, J. J.; Kaufman, T. M.; Sedlak, A. B.; Crook, M. F.; Alivisatos, A. P. Observation of ordered organic capping ligands on semiconducting quantum dots via powder X-Ray diffraction. *Nat. Commun.* **2021**, *12*, 2663.
(38) Yu, Y.; Luo, Z.; Chevrier, D. M.; Leong, D. T.; Zhang, P.; Jiang, D.; Xie, J. Identification of a Highly Luminescent $Au_{22}(SG)_{18}$ Nanocluster. *J. Am. Chem. Soc.* **2014**, *136*, 1246−1249.
(39) R Heath, J.; Shiang, J. J. Covalency in semiconductor quantum dots. *Chem. Soc. Rev.* **1998**, *27*, 65−71.
(40) Kim, Y.; Chang, J. H.; Choi, H.; Kim, Y. H.; Bae, W. K.; Jeong, S. III-V colloidal nanocrystals: control of covalent surfaces. *Chem. Sci.* **2020**, *11*, 913−922.
(41) Franke, D.; Harris, D. K.; Chen, O.; Bruns, O. T.; Carr, J. A.; Wilson, M. W. B.; Bawendi, M. G. Continuous injection synthesis of indium arsenide quantum dots emissive in the short-wavelength infrared. *Nat. Commun.* **2016**, *7*, 12749.
(42) Yu, P.; Beard, M. C.; Ellingson, R. J.; Ferrere, S.; Curtis, C.; Drexler, J.; Luiszer, F.; Nozik, A. J. Absorption Cross-Section and Related Optical Properties of Colloidal InAs Quantum Dots. *J. Phys. Chem. B* **2005**, *109*, 7084−7087.
(43) Kim, T.; Kelley, M. L.; Kim, D.; Greytak, A. B.; Jeong, S. Purification of Colloidal Nanocrystals Along the Road to Highly Efficient Photovoltaic Devices. *Int. J. Precis. Eng. Manuf.* **2021**, *8*, 1309−1321.
(44) Asor, L.; Liu, J.; Xiang, S.; Tessler, N.; Frenkel, A. I.; Banin, U. Zn-Doped P-Type InAs Nanocrystal Quantum Dots. *Adv. Mater.* **2023**, *35*, 2208332.
(45) Perdew, J. P.; Burke, K.; Ernzerhof, M. Generalized Gradient Approximation Made Simple. *Phys. Rev. Lett.* **1996**, *77*, 3865−3868.
(46) Blöchl, P. E. Projector Augmented-Wave Method. *Phys. Rev. B* **1994**, *50*, 17953−17979.
(47) Kresse, G.; Furthmüller, J. Efficient iterative achemes for *ab Initio* total-energy calculations using a plane-wave basis set. *Phys. Rev. B* **1996**, *54*, 11169−11186.
(48) Kresse, G.; Joubert, D. From ultrasoft pseudopotentials to the projector augmented-wave method. *Phys. Rev. B* **1999**, *59*, 1758−1775.
(49) Grimme, S.; Antony, J.; Ehrlich, S.; Krieg, H. A consistent and accurate *ab initio* parametrization of density functional dispersion correction (DFT-D) for the 94 Elements H-Pu. *J. Chem. Phys.* **2010**, *132*, 154104.
(50) Heyd, J.; Scuseria, G. E.; Ernzerhof, M. Hybrid functionals based on a screened Coulomb potential. *J. Chem. Phys.* **2003**, *118*, 8207−8215.
(51) Vydrov, O. A.; Heyd, J.; Krukau, A. V.; Scuseria, G. E. Importance of short-range versus long-range Hartree-Fock exchange for the performance of hybrid density functionals. *J. Chem. Phys.* **2006**, *125*, 074106.
(52) Casida, M. E.; Jamorski, C.; Casida, K. C.; Salahub, D. R. Molecular excitation energies to high-lying bound states from time-dependent density-functional response theory: Characterization and correction of the time-dependent local density approximation ionization threshold. *J. Chem. Phys.* **1998**, *108*, 4439−4449.
(53) Frisch, M. J.; Trucks, G. W.; Schlegel, H. B.; Scuseria, G. E.; Robb, M. A.; Cheeseman, J. R.; Scalmani, G.; Barone, V.; Petersson,

https://doi.org/10.1021/jacsau.3c00809
JACS Au 2024, 4, 1097−1106

G. A.; Nakatsuji, H.; Li, X.; Caricato, M.; Marenich, A. V.; Bloino, J.; Janesko, B. G.; Gomperts, R.; Mennucci, B.; Hratchian, H. P.; Ortiz, J. V.; Izmaylov, A. F.; Sonnenberg, J. L.; Williams-Young, D.; Ding, F.; Lipparini, F.; Egidi, F.; Goings, J.; Peng, B.; Petrone, A.; Henderson, T.; Ranasinghe, D.; Zakrzewski, V. G.; Gao, J.; Rega, N.; Zheng, G.; Liang, W.; Hada, M.; Ehara, M.; Toyota, K.; Fukuda, R.; Hasegawa, J.; Ishida, M.; Nakajima, T.; Honda, Y.; Kitao, O.; Nakai, H.; Vreven, T.; Throssell, K.; Montgomery, J. A., Jr.; Peralta, J. E.; Ogliaro, F.; Bearpark, M. J.; Heyd, J. J.; Brothers, E. N.; Kudin, K. N.; Staroverov, V. N.; Keith, T. A.; Kobayashi, R.; Normand, J.; Raghavachari, K.; Rendell, A. P.; Burant, J. C.; Iyengar, S. S.; Tomasi, J.; Cossi, M.; Millam, J. M.; Klene, M.; Adamo, C.; Cammi, R.; Ochterski, J. W.; Martin, R. L.; Morokuma, K.; Farkas, O.; Foresman, J. B.; Fox, D. J. *Gaussian 16*, Revision C.01; Gaussian, Inc.: Wallingford, CT, 2016.

(54) Farrow, C. L.; Billinge, S. J. L. Relationship between the atomic pair distribution function and small-angle scattering: implications for modeling of nanoparticles. *Acta Crystallogr., Sect. A: Found. Crystallogr.* **2009**, *65*, 232−239.

(55) Brown, P. J.; Fox, A. G.; Maslen, E. N.; O'Keefe, M. A.; Willlis, B. T. M.. In *International Tables for Crystallography: Mathematical, Physical and Chemical Tables*; Prince, E., Ed.; Wiley, 2004; Vol. *C*, pp 544−595.

https://doi.org/10.1021/jacsau.3c00809
JACS Au 2024, 4, 1097−1106